

Quantitative Atomic Spectroscopy for Primary Thermometry

Gar-Wing Truong,^{1,*} Eric F. May,² Thomas M. Stace,³ and André N. Luiten¹

¹*Frequency Standards and Metrology Research Group, School of Physics,
The University of Western Australia, Perth, WA 6009, Australia*

²*Centre for Energy, School of Mechanical and Chemical Engineering,
The University of Western Australia, Perth, WA 6009, Australia*

³*School of Mathematics and Physics, University of Queensland, Brisbane, QLD 4072, Australia*

(Dated: November 8, 2019)

Quantitative spectroscopy has been used to measure accurately the Doppler-broadening of atomic transitions in ^{85}Rb vapor. By using a conventional platinum resistance thermometer and the Doppler thermometry technique, we were able to determine k_B with a relative uncertainty of 4.1×10^{-4} , and with a deviation of 2.7×10^{-4} from the expected value. Our experiment, using an effusive vapour, departs significantly from other Doppler-broadened thermometry (DBT) techniques, which rely on weakly absorbing molecules in a diffusive regime. In these circumstances, very different systematic effects such as magnetic sensitivity and optical pumping are dominant. Using the model developed recently by Stace and Luiten, we estimate the perturbation due to optical pumping of the measured k_B value was less than 4×10^{-6} . The effects of optical pumping on atomic and molecular DBT experiments is mapped over a wide range of beam size and saturation intensity, indicating possible avenues for improvement. We also compare the line-broadening mechanisms, windows of operation and detection limits of some recent DBT experiments.

I. INTRODUCTION

An ability to measure absolute thermodynamic temperature is currently confined to an exclusive list of national standards laboratories. Such measurements require primary thermometry expertise and highly specialised equipment, making it impractical for wider-scale use. Instead, for practical purposes, temperature scales such as ITS-90 [1], are used as an approximation to the true thermodynamic temperature, even though they are known to have relative uncertainties at the 10^{-4} level [2]. Accordingly, there is now a global push to develop more convenient methods of primary thermometry that could make thermodynamic temperature measurements more broadly available [3]. A second motivating factor driving recent renewed interest in primary thermometry is the call by the Bureau des Internationale de Poids et Measures' to remeasure the Boltzmann constant, k_B , using a wide range of techniques in preparation for the redefinition of the kelvin in 2011 [4, 5].

At present, the recommended value for k_B is derived primarily from one acoustic measurement performed by Moldover *et. al.* [6]. It would be preferable if k_B could be remeasured using different methods with comparable uncertainties so that any systematic errors can be identified. Recently, Bordé suggested that the known[7] temperature dependence of the spectral linewidth of absorption features, previously exploited for measurements of stellar atmospheric temperatures[8], can be used as a new technique for accurate primary thermometry[9]. This Doppler-broadening thermometry (DBT) method has since been experimentally realized and while currently less precise than other primary methods such as

acoustic or dielectric constant gas thermometry, it suffers from very different types of systematic errors [10]. In contrast to those techniques which measure the macroscopic quantity RT , the DBT method can directly probe the microscopic thermal energy $k_B T$ by measuring the characteristic spectral width of molecular/atomic transitions, thereby avoiding the uncertainties in the Avogadro constant N_A .

The first DBT measurements performed by Daussy *et. al.* and Casa *et. al.* have used molecular gases at 1-130 Pa and determined k_B with a relative uncertainty [11–13] of order 10^{-4} . More recent work has improved the statistical uncertainty [14] to 4×10^{-5} . In this paper, we present results from an atomic Rubidium (Rb) DBT system at 3×10^{-5} Pa. The use of an alkali metal atom absorber presents some distinct spectroscopic differences that allow us to explore new experimental regimes within the DBT method. In doing so, we have identified some advantages in using an atomic system and encountered new challenges whose resolutions demand a deep understanding and detailed unification of light-matter interactions and gas dynamical theories [15]. Whilst this work has been motivated by primary thermometry, we believe that it has wider implications in all fields requiring high-resolution or precision, quantitative spectroscopy.

The primary difference between a low-pressure atomic vapor system, like Rb, and molecular experiments is that atomic motion is effusive, so collisions are extremely rare. An advantage of moving to this effusive regime is the avoidance of pressure-induced systematic changes, such as collisional line-shape perturbations [16]. This removes the need to extrapolate results to an equivalent zero-pressure value. Further, by using a sealed vapor-pressure reference gas cell, we avoid any unintended pressure drifts associated with a more sophisticated variable-pressure gas chamber. In this study, we chose Rb which has a

* Gar-Wing.Truong@physics.uwa.edu.au

high optical cross section, ensuring that the absorption signal-to-noise is satisfactory in spite of the very low vapor density. This choice also gives the ability to operate in a range where high quality lasers are readily available and where silicon detectors, with their extremely good linearity [17] and quantum efficiency, can be used. At room temperature, it was possible to use a smaller cell than those in the molecular experiments for the same absorption depth, which was convenient for thermal control.

On the other hand, there are also disadvantages to using atomic vapors. Care is required to ensure low levels of residual magnetic fields which can lead to the broadening of spectral lines by lifting the degeneracy of Zeeman levels. In the transition used in this experiment ($D2$ line of ^{85}Rb), optical pumping between unresolved hyperfine transitions contributed the greatest potential for systematic error by perturbing the lineshape. In addition, the comparability of the natural lifetime, beam transit time and the Rabi period in our situation leads to optical pumping effects that requires either an accurate model of the gas kinetics [15] or the use of a low power probe beam to avoid lineshape perturbations. We followed the second route here and show here that the resulting perturbation is at the 4 parts-per-million (ppm) level. We note, however, that it should be possible to operate at higher power levels and use the model of Stace and Luiten [15] to correct the results.

The remainder of this paper is organised as follows. In Sec. II, we describe the experimental setup and data acquisition for a Rb DBT experiment. The theoretical absorption coefficient lineshape for unperturbed atoms and the derivation of a suitable lineshape profile for extracting the quantity $k_B T$ from the acquired spectra are then described in Sec. III. Our experimental results are presented in Sec. IV, followed by a discussion about systematic uncertainties in Sec. V. In Sec. VI, we discuss the relative merits and challenges of the atomic approach in more detail. We will also discuss how the use of atomic vapors might be extended to a wider temperature range.

II. METHOD AND EXPERIMENT

A schematic of the experimental setup used in this work is shown in Fig. 1. The $k_B T$ product was determined from spectroscopic measurements of unresolved hyperfine transitions (from the $5^2S_{1/2}$, $F = 2 \rightarrow 5^2P_{3/2}$, $F = 1, 2, 3$ states) in the $D2$ line of ^{85}Rb at 780 nm. A custom-built extended cavity diode laser (ECDL) was locked to a tunable optical Fabry-Pérot cavity (OC) using the Pound-Drever-Hall (PDH) technique [18], which suppressed acoustic and other fluctuations of the laser frequency. We tuned the laser's wavelength by changing the length of the cavity. A sweep generator (Sweep) was used to displace one of the OC cavity mirrors by driving a piezo-electric stack actuator (PZT). A step-wise sweep was used to reduce the asynchronicity be-

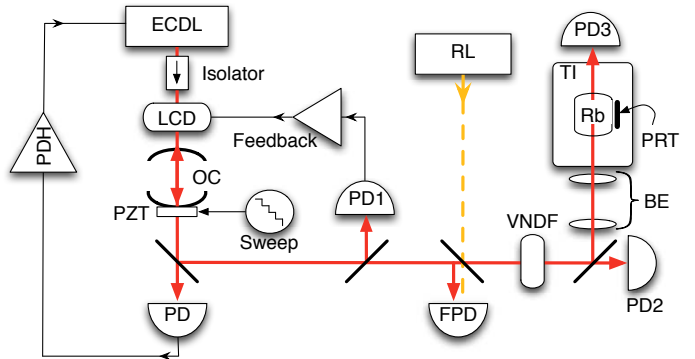


FIG. 1. (Color Online) A schematic diagram of the optical circuit and electronic control systems. ECDL: extended cavity diode laser; LCD: variable optical depth liquid crystal display; OC: optical cavity; PZT: annular piezo-electric stack; PDH: Pound-Drever-Hall top-of-resonance feedback control loop; RL: reference laser; VNDF: variable neutral density filter; BE: beam expander lenses; PRT: ITS-90 calibrated platinum resistance thermometer; TI: thermal isolator; (F)PD: (fast) photodetector.

tween measurements of the temperature, frequency and absorbed power. An LCD variable optical attenuator was used to keep the intensity transmitted through the cavity, which was monitored by the photodetector PD1, at a constant. This suppressed variations in the amount of optical pumping associated with power changes occurring throughout the scan.

The optical frequency difference between the probe and a reference laser (RL) was measured using a fast photodetector (FPD) and a high bandwidth counter. The reference beam was derived from a tunable Ti:Sapphire laser locked to a temperature-controlled, ultra-low expansion optical cavity. The stability of the reference laser (~ 1 kHz) contributed negligible uncertainty to the optical frequency measurement. A variable neutral density filter (VNDF) allowed measurements to be made at incident probe powers below that set by the LCD intensity control system, without affecting intensity or frequency stabilities. A photodetector (PD2) located just before the absorption cell was used to correct for any residual probe power changes. A beam expander (BE) was used to give the largest beam possible through the cell (2 cm in diameter) to maximise the input power for a given intensity to achieve a high signal-to-noise ratio. The power transmitted through a 10 cm long Rb absorption cell was measured on a third photodetector (PD3). The Rb cell was encased in a passive thermal isolator (TI) whose temperature was monitored using a using a platinum resistance thermometer (PRT) calibrated to ITS-90 with 30 mK uncertainty. The maximum temperature difference across the isolator was measured to be less than 7 mK using auxiliary thermometers (not shown). The thermal relaxation time constant of the isolator (~ 2 hours) was much larger than the time required for a single sweep (10 mins).

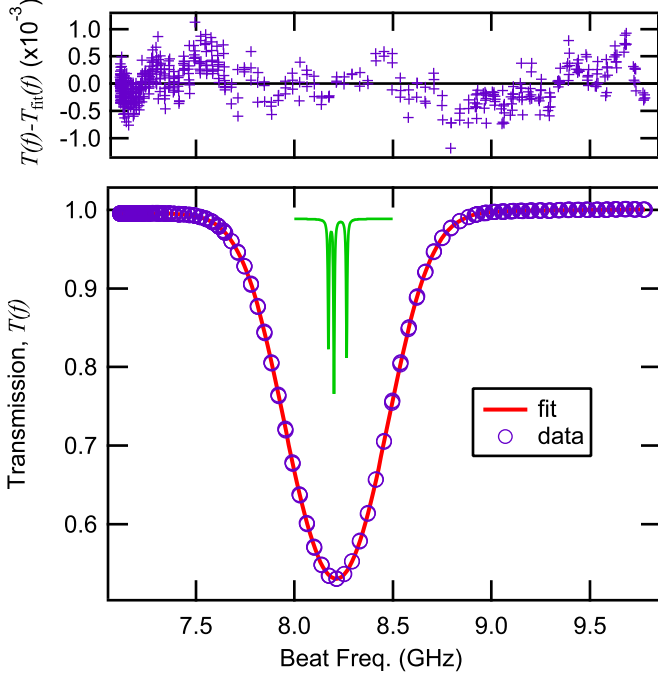


FIG. 2. (Color online) The lower panel shows a typical spectrum (blue circles) obtained from Rb vapour at 295 K (~ 550 points) and the fit (red) using Eqn. (2). The Lorentzians (green) indicate both the location of the underlying hyperfine transitions and their relative strengths (in arbitrary units). The upper panel displays the residuals to the fit.

The outputs of PD2 and PD3 that monitored the incident probe and the transmitted powers, respectively, were recorded using digital multimeters with 5-digit resolution. A third multimeter was used to make four-wire resistance measurements of the PRT. A computer-based data acquisition system centrally controlled and logged the three digital multimeters and the high bandwidth counter outputs. Before each set of measurements at a fixed probe power level, the DC voltages on PD2 and PD3 caused by stray lights, were recorded in the absence of the probe beam. These backgrounds were removed from the detector readings before reconstructing the Doppler-broadened absorption spectrum by dividing the output of PD3 by that of PD2.

III. EXTRACTING $k_B T$ FROM SPECTRA

In a low density gas cell, the absorption coefficient of an isolated spectral line is the convolution between a Lorentzian and a Gaussian function, known as a Voigt profile [7]. The Lorentzian component can be written as $L(\nu) = (1 + [(\nu - \nu_0)/\Gamma]^2)^{-1}$, where ν is the optical frequency and ν_0 is the atomic transition frequency. This component arises from the finite lifetime of the upper state and has a full-width-at-half-maximum (FWHM) of $\Gamma = 1/(2\pi\tau)$, where τ is the total upper state life-

time. Various phenomena including collisional, transit time and power broadening can perturb the width of this Lorentzian. It was important in this experiment to keep these perturbations at negligible levels.

The Gaussian component has the form of $G(\nu) = \exp(-[(\nu - \nu_0)/\Delta\nu_D]^2)$, where the $1/e$ -half-width of the Gaussian component is related to the thermal energy $k_B T$ as:

$$k_B T = \frac{mc^2}{2} \left(\frac{\Delta\nu_D}{\nu_0} \right)^2 \quad (1)$$

and arises from the thermal motion of the atoms. Here c is the speed of light, m is the mass of the absorbing atom and ν_0 is the absolute transition frequency. For Rb, the latter two parameters are known with relative uncertainties of 5×10^{-8} and 5×10^{-11} , respectively [19, 20], which are negligible for this experiment. Whilst it was possible to compute the absorption coefficient $V(\nu, \Delta\nu_D) = L(\nu) \otimes G(\nu)$ by performing a convolution integral, this was a computationally inefficient procedure. Instead, a numerical routine described by Humlcek [21] implemented in the scientific data analysis program *Igor Pro*[22] was used to generate the Voigt function. The relative accuracy of this algorithm was better than 3×10^{-5} and no consideration of these numerical errors was required in the following analysis.

The observed transmission spectrum was determined by Beer's Law [7], $T(\nu) = \exp(-V(\nu, \Delta\nu_D)L)$, where L is the optical path length of the probe inside the absorbing gas. Since this experiment concerns frequency differences, it was convenient to shift the frequency origin by subtracting away the absolute optical frequency of the $^{87}\text{Rb } F = 2 \rightarrow 1$ hyperfine transition. We denote these frequency differences with f to avoid confusion with the absolute frequencies ν . We performed least-squares regression of the transmission spectra to Eqn. (2) to determine $\Delta\nu_D$.

$$T(f) = A f + B \exp \left(-C \sum_{i=1}^3 S_i V_i(f - f_i - f_{\text{cav}}, \Delta\nu_D) \right) \quad (2)$$

Here, $T(f)$ is the sum of three, unresolved hyperfine transitions, indicated schematically in Fig. 2; the $V_i(f - f_i - f_{\text{cav}})$ are the Voigt functions corresponding to each hyperfine transition, each centered on frequency f_i and with relative strength S_i ; and A , B and C are three of the five parameters adjusted in the regression. The S_i were fixed at values derived from the Clebsch-Gordan coefficients while the f_i were fixed at values determined by Arimondo *et. al.* [20]. Of the adjustable parameters, A and B account for, respectively, a residual background and imperfect background normalisation (to a value of 1) of the spectra. C is the on-resonance absorption depth determined by the number density and the cell length. The two other adjustable parameters, f_{cav} and $\Delta\nu_D$ were contained within, and were common to the three Voigt functions, with f_{cav} allowing for the arbitrary (but fixed) frequency offset of the reference laser from the lowest

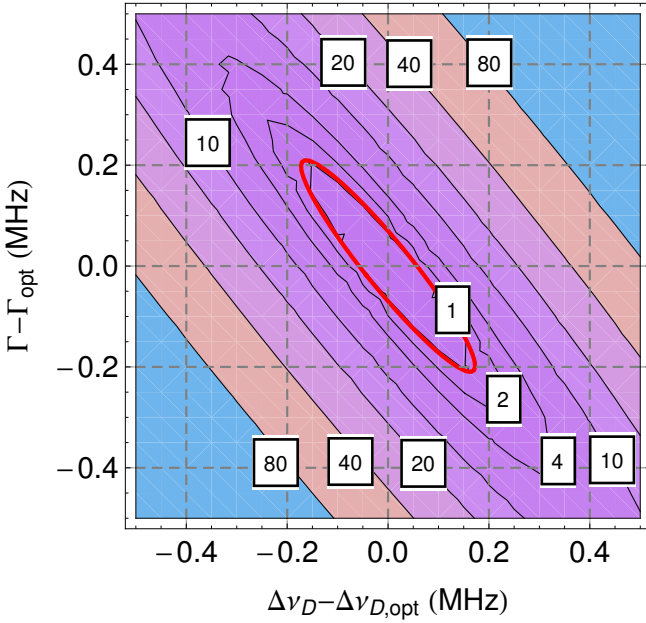


FIG. 3. (Color Online) The $(\chi^2 - \chi^2_{\text{opt}})$ -surface as a function of change in Lorentzian and Gaussian widths, denoted $\Gamma - \Gamma_{\text{opt}}$ and $\Delta\nu_D - \Delta\nu_{D,\text{opt}}$ respectively, show that there is a high degree of correlation between these fit parameters. The subscripts opt denote the optimum quantities determined from the least-squares fit, which were 2.75 MHz and 308.0 MHz, for the Lorentz and Gaussian widths, respectively. The thicker, red contour is generated from the covariance matrix and is intended to guide the eye.

frequency hyperfine line. The Gaussian width $\Delta\nu_D$ was converted to $k_B T$ using Eqn. (1).

In principle, it is possible to perform the regression allowing every parameter in Eqn. 2 to be adjustable. However, in this case, the returned parameters from the least-squares fit show strong correlations between a number of the free parameters. This leads a larger uncertainty range in those parameters. In particular, we find strong correlations in the S_i , and also in Γ and $\Delta\nu_D$ which have a correlation coefficient of -0.96. Operating in an intensity range where it is possible to fix the Lorentz width and the strengths S_i to known values, we avoid an artificial inflation of the uncertainties associated with the fitted Doppler width due to these correlations. Our theoretical model (see Section V) guides us on the upper intensity.

IV. RESULTS

The results from several k_B determinations are shown in Fig. 4 as a function of incident probe power. These data were produced from 24 spectra taken at intensities at least 500-fold below the saturation intensity [23] ($I_{\text{sat}} \sim 20 \text{ W/m}^2$). The total uncertainties at each power level are indicated by the error bars and were determined from the standard deviation of the data sets taken at the same power level. Our final determination of the Boltz-

TABLE I. Values of the fixed constants used in Eqn. 2 for the relative transition strengths, S_i , and their frequency offsets [20], f_i . The relative transition strengths are exact numbers, whilst there is a relative uncertainty of order 1×10^{-5} associated with the differences between the hyperfine transition frequencies.

$F_{\text{upper}} = i$	S_i	f_i (MHz)
1	1/3	4372.399(85)
2	35/81	4401.771(37)
3	28/81	4465.172(53)

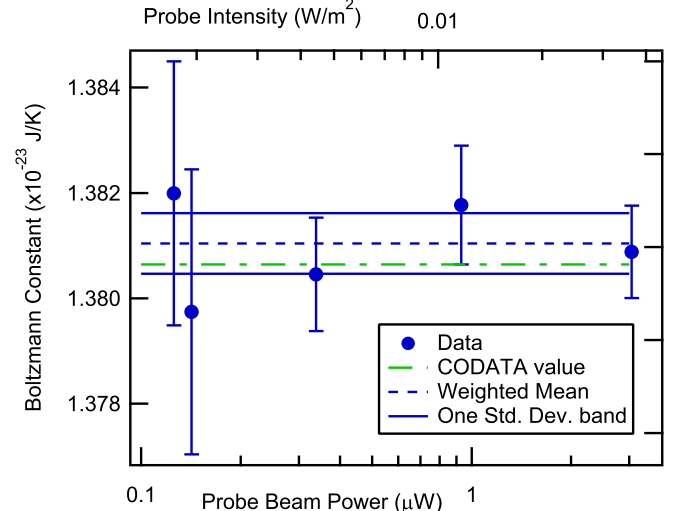


FIG. 4. (Color Online) The value of k_B (dots) extracted from fitting spectra measured at several probe powers. The weighted mean (blue dashed) and weighted one-standard-deviation band (blue solid) are shown. The green, dot-dashed line is the CODATA [6] value.

mann constant, based on a weighted mean of the measurements at the various probe powers, is

$$k_B = 1.38104(59) \times 10^{-23} \text{ J/K.}$$

The uncertainty in this measurement was limited primarily by residual amplitude noise at frequencies higher than the bandwidth of the LCD feedback control loop. This white noise was exacerbated by a lower than expected common-mode rejection of amplitude noise resulting from some asynchronicity in the data acquisition scheme.

The broadening of the Lorentzian linewidth by magnetic fields contributed a smaller systematic uncertainty of 9.8×10^{-5} , which was summed in quadrature give a total relative uncertainty of 4.1×10^{-4} . All other systematic uncertainties were kept at negligible levels and will be discussed in the following section. However, as the random uncertainties and measurement timing are addressed in future work, these will become increasingly important. Our value of k_B has a relative deviation of

2.7×10^{-4} from the current CODATA value. To our knowledge, this is the most accurate demonstration of primary thermometry using spectroscopy of *atomic* absorbers.

V. ESTIMATION OF SYSTEMATIC UNCERTAINTIES

The greatest source of systematic uncertainty in this experiment was caused by the Earth's magnetic field. This external field lifted the frequency degeneracy of the Zeeman sub-levels in the Rb hyperfine transitions. The field along the cell was measured to be $0.21(1)$ G and numerical simulations shows that this causes an apparent broadening of the Lorentzian linewidth by 0.5%, which in turn, contributes a relative uncertainty of 9.8×10^{-5} in the measured value of k_B . Whilst magnetic shields can be used to reduce the field strength by a factor of 40 000 times, this was not attempted because the effect was smaller than the observed random uncertainties of the experiment.

The Rb spectra were recorded (non-contiguously) over a one month period. Whilst no drift would be expected from the use of a permanently sealed Rb vapor-pressure reference cell with no buffer gas, checks for long-term stability were performed by periodically re-acquiring spectra at previously investigated probe power levels. We detected no long term drift larger than the short-term reproducibility of the experiment. A long-term drift of the reference laser's wavelength only changes the fitted offset frequency f_0 but does not change the Rb spectrum and is therefore inconsequential.

We also considered the systematic uncertainty caused by holding Γ and S_i constant. Fig 3 demonstrates that the minimum of the χ^2 surface lies along $(\Gamma - \Gamma_{\text{opt}})/(\Delta\nu_D - \Delta\nu_{D,\text{opt}}) \approx 1$, so the propagated relative uncertainty in $\Delta\nu_D$ due to the uncertainty of Γ is reduced by a factor $\sim \Delta\nu_D/\Gamma \approx 100$. Since the unperturbed Lorentzian width is known [24] with a relative uncertainty of 3×10^{-4} , this contributes a negligible uncertainty in $\Delta\nu_D$. Similarly, there is no uncertainty associated with the transition strengths because they are exact numbers. However, these assumptions are valid only in the limit of zero probe beam power because the measurement process itself can perturb the actual values of Γ and S_i away from their theoretical values. For example, excess probe beam power will lead to power-broadening of the underlying Lorentzian linewidth, introducing an intensity dependence in the fitted Doppler width and, thus, in k_B . Similarly, any optical pumping between the hyperfine states that produces alignment or polarization of the sample will perturb the effective ratios S_i/S_j . We did indeed observe such effects at intensities greater than ~ 1 W/m² (at least 30 times larger than intensities reported here), which is still more than an order of magnitude below the saturation intensity [23].

We have developed a new theory [15] to explain the

TABLE II. Different experimental regimes accessed by various choices of absorbers. The relative noise reported in the bottom two rows are given for a 1000 s bandwidth.

	Rb	NH ₃ [11]	CO ₂ [12]
Doppler Width (MHz)	308	50	275
Pressure (Pa)	10^{-5}	8	130
Pressure Broadening (MHz)	0.02	1	4
Optical Pumping, \mathcal{F}	0.021	8×10^{-8}	3×10^{-7}
Probe Power (μ W)	0.1	0.1	50
1000 s Shot Noise Floor (ppm)	0.7	0.8	1.2
1000 s Achieved Reproducibility (ppm)	4000	1000	200

cause of this early onset of optical saturation behaviour which allows us to confirm that a negligible amount of optical pumping occurred in the experiments reported here. In contrast to previous models [17, 25, 26] that approximate the atom as a two-level system under uniform illumination, we developed a theory for multi-level atoms probed by a beam with finite spatial extent [15]. This better captures the physical properties and situation of this Rb experiment. We find that the saturation-like behaviour came from an optical pumping process that evacuated the population in the laser-coupled ground state, and not from a Rabi-flopping mechanism responsible for saturation in a two-level system [7, 27]. We, therefore, quantify the perturbation away from thermal equilibrium by introducing a figure-of-merit, denoted \mathcal{F} , defined as the relative depletion of the laser-coupled ground state, i.e.

$$\mathcal{F} \equiv 1 - \frac{\rho_1}{\rho_{1,\text{th}}} \quad (3)$$

where $\rho_{1,\text{th}}$ and ρ_1 are the thermal and pumped fractional occupation of the ground state. In the absence of optical pumping ($\rho_1 = \rho_{1,\text{th}}$), $\mathcal{F} = 0$; whilst conversely, when the ground state is fully depleted, ($\rho_1 = 0$) and $\mathcal{F} = 1$. Using the full model of Stace and Luiten [15], we computed the figure-of-merit to be $\mathcal{F} \approx 0.021$ for the largest powers in this experiment. In Appendix A, we show how \mathcal{F} may be calculated approximately using a simple method based on conservation of energy considerations. At $\mathcal{F} = 0.021$, the perturbation in k_B due to optical pumping is 4 ppm (see Appendix B), which is well below the current statistical uncertainty. We also showed experimentally that we were sufficiently close to the zero-probe-power limit by demonstrating the absence of any statistically significant slope in the deduced value of k_B as a function of power on Fig. 4.

VI. COMPARISON TO MOLECULAR DBT

In this section, we will highlight the differences between a low-pressure atomic approach and high-pressure molecular DBT experiments by examining reported results, simulated spectra and the results presented in Sec-

tion IV. Table II shows a comparison of some recent DBT experiments using molecules and atoms.

A. Shot-noise limits

Using the probe powers shown in Table II, row 5, we simulated shot-noise limited Doppler-broadened spectra consisting of 1000 absorbance samples spanning $f_0 \pm 3\Delta\nu_D$. An approximate estimate of the shot-noise limited relative uncertainty of k_B was found by fitting these spectra to our model. The results are surprisingly similar for all experiments (row 6). The results depend mostly on the total scan time and not details such as the frequency spacings between points. Despite the high CO₂ probe power reported in Ref. [12], the shot-noise limit is similar to the other experiments because of the low absorption depth in that experiment. The last row of Table II shows that the approximate actual repeatability calculated from reported results, when scaled to 1000 s time scale, is significantly worse than the shot-noise limit in all cases. Djerrood *et. al.* [14] have reported recent improvements to the work of Daussy *et. al.* by achieving a reproducibility of 100 ppm at 1000 s. In our case, we found that background light levels have a significant impact on experimental repeatability, so we intend in future experiments to employ synchronous detection of a modulated carrier. Preliminary results suggest this improves the repeatability to 150 ppm.

B. Exploration of a Different Spectroscopic Regime

When examining the pressure differences in current DBT experiments, at 10^{-5} Pa, the gas dynamics of a Rb vapor is governed by an effusive flow of atoms, i.e. the system is essentially collisionless and the trajectory of any atom is completely determined (until it hits the cell wall) given a velocity at any particular instant. This leads to negligible pressure-induced self-broadening [7]. In contrast, collisions are dominant in the diffusive regime of the molecular DBT experiments causing $\sim 0.01\Delta\nu_D$ of pressure-related broadening [11, 28]. Moreover, the physical details of the molecule-molecule collisions are critical in determining the observed line-shape profile. For example, the degree of elasticity of molecular collisions perturbs the lineshape away from a Voigt profile [16]. This requires higher-order forms such as the Galatry profile and a greater number of adjustable parameters required for the regression of spectra.

To compensate for the much lower density in the atomic vapors, it was necessary to use strongly absorbing atoms (such as the alkalis). As is evident from row 4 of Table II, this results in larger optical pumping of the atomic system and care is required to account for systematic errors arising therefrom. To illustrate the very different operational spectroscopic regimes interrogated in this work and by Daussy *et. al.* [11, 14] and Casa *et.*

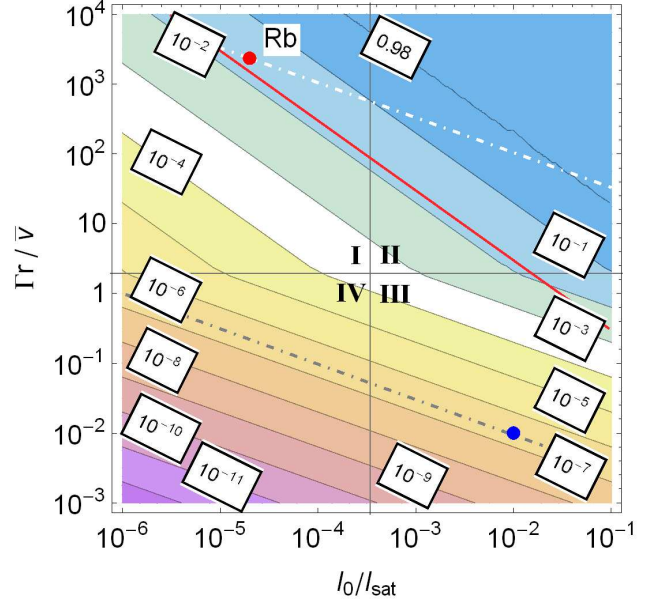


FIG. 5. (Color Online) A contour plot of \mathcal{F} computed a simple model of a three level atom in a Λ configuration, as a function of probe power normalised to the saturation intensity and normalised beam-transit time. The red and blue dots indicate the conditions of this and the molecular DBT experiments, respectively, demonstrating the exploration of vastly different spectroscopic regimes. The dot-dashed lines are contours of constant *input* power. The solid red line indicates the experimental conditions that would lead to a 1 ppm perturbation in k_B .

al. [12, 13], Fig. 5 shows a contour plot of an estimate of \mathcal{F} as a function of the non-dimensional intensity [23], $I_0/I_{\text{sat}} \equiv 2\Omega^2$ and the normalised, characteristic beam crossing time $\Gamma r/\bar{v} \equiv t^*$ where $\bar{v} = \sqrt{2kT/m}$ is the mean atomic speed and r is the beam radius.

The estimate for \mathcal{F} is based on a very simple model of a three level atom in a Λ configuration, subject to a driving field with Rabi frequency $\Omega = \Omega^* \Gamma$ resonant with one of the transitions for a length of time $t = r/\bar{v} = t^*/\Gamma$, and relaxation at a rate $\Gamma/2$ from the excited state to each of the two ground states. It is simple to show that

$$\mathcal{F} \approx \begin{cases} (\Omega^* t^*/2)^2 & \text{if } t^* \gg 2 \\ \Omega^{*2} t^*/2 & \text{if } t^* \ll 2 \end{cases}, \quad (4)$$

and it is this function whose contours are plotted in Fig. 5. This simple model gives a reasonable estimate of \mathcal{F} , which can be refined using more sophisticated models capable of predicting \mathcal{F} quantitatively [15].

To aid discussion, we have divided Fig. 5 into quadrants labelled I through IV. These quadrants correspond to different regimes of signal-to-noise ratio (SNR), optical pumping and dependence on beam geometry. In the upper half of Fig. 5 (quadrants I and II), where $\Gamma r/\bar{v}$ is greater than ≈ 2 , the contours of constant \mathcal{F} have a slope of -1 decade/decade. In the lower half, where the

transit time (r/\bar{v}) is smaller than the upper state lifetime ($\tau = 1/\Gamma$), lines of constant \mathcal{F} have slope $-1/2$ decade/decade. Since the input intensity I_0 is proportional to r^{-2} , contours of constant *input* power have slope $-1/2$ decade/decade. Two such contours (dot-dashed) are drawn through the location of the Rb experiment reported here as well as the molecular experiments. Contours of constant *absorbed* power follow lines of constant \mathcal{F} since the absorption coefficient is proportional to the population perturbation in the ground state, i.e.

$$V(f_i, \Delta\nu_D) \approx \rho_1 = \rho_{1,\text{th}}(1 - \mathcal{F}). \quad (5)$$

Our Rb experiment is located in quadrant I, which is characterized by low probe power and where \mathcal{F} is mostly between 10^{-5} and 10^{-1} . In this quadrant, the slope of a line of constant input power (dot-dashed lines) differs from lines of constant absorbed power (constant \mathcal{F}). Therefore, a compromise is required between using a low power probe beam to access a regime of smaller \mathcal{F} and using higher powers to mitigate detector noise. For example, traversing a line of constant incident power in the direction of increasing I_0/I_{sat} causes the Rb experiment to sample larger \mathcal{F} values, which in turn, causes a reduction in the absorption coefficient in accordance with Eqn. 5. Using the analysis of Appendix B, the solid red line indicates the parameters where there is a 1 ppm perturbation to the determination of k_B . Clearly, quadrant II is not a desirable regime to operate for Doppler thermometry because the high probe powers lead to intolerable amounts of lineshape perturbation by optical pumping.

In the case of the molecules (quadrant III), there is little optical pumping since \mathcal{F} is small, due to a small optical cross-section (small Γ). The contours of constant input and absorbed power have the same slope and, therefore, the beam geometry plays no part

Given ideal detectors, operating in quadrant IV would be optimal; however, doing so is impractical given the small interaction cross-sections and their impact on SNR. The challenges faced by experiments located in quadrants III and IV can be illustrated by considering the shot-noise limited SNR:

$$\text{SNR} \propto \frac{I_0 \exp(-\alpha l)}{\sqrt{I_0}} = \sqrt{I_0} \exp(-\alpha l), \quad (6)$$

where the numerator is the scattered intensity and the denominator is proportional to the shot-noise. The absorption coefficient can be written as [27]

$$\alpha = \sigma_0 \rho_0 \propto \Gamma \lambda^2 P, \quad (7)$$

where σ_0 , ρ_0 and P are the optical cross-section, number density and pressure of the absorber, respectively. We can more clearly see the trade-offs of operating in quadrants III and IV by writing an “equation of state” for the SNR,

$$\ln(\text{SNR}) \sim \left(\frac{(\lambda/\text{nm})^2}{780^2} \right) \left(\frac{\Gamma/\text{s}^{-1}}{4 \times 10^7} \right) \left(\frac{P/\text{Pa}}{3.5 \times 10^{-5}} \right) \left(\frac{l/\text{m}}{10^{-2}} \right). \quad (8)$$

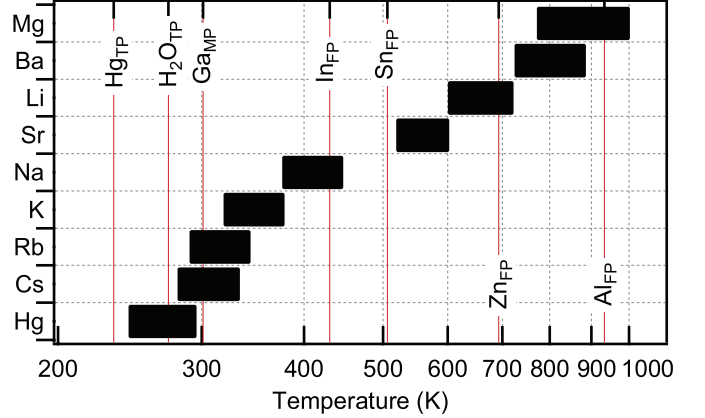


FIG. 6. (Color online) Approximate temperature windows of operation for various vapor-pressure cells, of length restricted to 10 cm. The species in each cell is shown on the vertical axis. The temperatures of selected ITS-90 fixed points are indicated by the solid vertical red lines. The subscripts TP, MP and FP denote Triple Point, Melting Point and Freezing Point, respectively.

To achieve comparable SNR to atomic absorbers in which Γ is large, molecular-based approaches require the product of P and l to be large in compensation. Either of these requirements have problematic impacts on k_B measurements related to pressure-broadening and thermal control, respectively.

Whilst it was possible in the Rb experiment to explore a region of smaller \mathcal{F} by reducing the input power (e.g. moving vertically downwards in Fig. 5 by decreasing r for a set value of I_0/I_{sat}), it was not feasible to reach a value equivalent to those achieved by the molecular experiments ($\sim 10^{-7}$) because of the rapid decrease in SNR. Similarly, the molecular experiments cannot access the strong pumping regime since it requires ~ 100 -fold increase in the beam radius to do so. Perhaps operating at the geometric mean of the extremes defined by the existing experiments might provide simultaneous insensitivity to pressure related and optical pumping effects. For example, there are a series of suitable transitions between 311 nm and 323 nm in Rb. In particular, the 315.75 nm transition [29] of Rb has $\Gamma = 3.4 \times 10^4$, which is approximately 1000 times less absorbing than the lines used in this study.

C. Windows of Operation

In this experiment, we used a commercially available Rb vapor cell of a standard length (10 cm), which gave an absorption depth of $\sim 50\%$ at room temperature. However, operating at the equilibrium vapor pressure means that the number density is more sensitive to temperature than in the molecular experiments. The range of temperatures over which we can use Rb as a thermometric substance is comparatively smaller than for molecules.

The lower temperature bound is provided by the rapidly diminishing absorption depth. The upper bound is set by the severe extinction in probe power in a large frequency region about atomic resonance, causing the line-shape to resemble a step-function. Fig. 6 shows approximate temperature windows over which a selection of metal gases at their vapor pressure might be able to operate [23, 30–36]. At the upper and lower temperature bounds of each window, the noise on the fitted Doppler width would double from its optimum value. We have restricted attention to 10 cm long cells for convenient thermal control. Some fixed points of the ITS-90 [10] scale are also shown, demonstrating that metallic vapor-pressure DBT can be used to verify the thermodynamic temperature at those fixed points. For a particular choice of absorber, it is also possible to fill the reference cell using an external atomic reservoir at a lower temperature, resulting in a lower vapor number density. Once the vapor cell is sealed, no further increase in number density would be possible, thereby restricting optical depth to an optimum level when at high temperatures.

VII. CONCLUSIONS

Doppler broadening thermometry provides a significantly different approach to the determination of the Boltzmann constant in preparation for the re-definition of the kelvin. Whilst previous DBT experiments have studied molecular absorbers at up to 10 Pa in a diffusive regime, we have used Rb at 0.001 Pa where the gas dynamics are effusive. Our approach avoids problems such as pressure broadening and poor signal-to-noise. Furthermore, the Rb cell is compact in size, enabling more convenient temperature control. We used this system to determine k_B with a relative uncertainty of 4×10^{-4} . The present experiment was limited by amplitude noise in the probe beam, which in future work will be overcome by using a control loop with larger bandwidth. We estimate that all current DBT experiments are far from the shot noise limit and that the use of synchronous detection methods could address this situation.

We also compared sources of systematic uncertainty for DBT experiments in the diffusive regime of molecular DBT and the effusive regime of atomic DBT. For atomic vapors such as Rb, the shift in the determined value of k_B due to the Earth's magnetic field is approximately 100 ppm. Optical pumping effects are determined by the combination of beam transit time, upper-state lifetime and probe intensity. In this work, the equilibrium ground-state population was perturbed by 0.2% which shifted the measured k_B value by 4 ppm. The small cross-sections of the transitions used in molecular DBT experiments means that the optical pumping effects are relatively small (perturbation to equilibrium ground-state population of order 10^{-7}). However, these small cross-sections mean that an equivalent signal-to-noise in molecular experiments requires long path lengths and/or

higher pressures, both of which have associated systematic effects on measurements of k_B . The method developed here for quantifying optical pumping effects can be used to search for candidate absorbers optimally suited to DBT experiments in either the diffusive or effusive regimes.

Appendix A: Approximate method for calculating \mathcal{F}

Whilst the approach of Stace and Luiten [15] captures the details of the gas-dynamical interaction between atoms and the beam volume, which can be used to estimate the population perturbation using no phenomenological parameters, it relies on a knowledge of the dipole matrix element in order to calculate the Rabi frequency. It is useful to compare this against a simpler, independent analytic calculation. We provide such a calculation here, based on energy conservation and using an *a posteriori* knowledge of the optical depth.

Assuming that the input intensity is sufficiently weak so that an atom never absorbs more than one photon during a single transit of the beam, the rate of atoms scattered out of the laser-coupled ground state is approximately the same as the rate of scattered photons. This is given by

$$R = a \frac{I_0}{E_\gamma} (1 - I/I_0), \quad (A1)$$

where $a = \pi r^2$ is the cross-sectional area of a beam with radius r , E_γ is the photon energy and I and I_0 are the *on-resonance* output and input intensities.

Using kinetic theory [37], the flux of atoms crossing the beam surface (of area $A = 2\pi r l$, where l is the cell length) is

$$\Phi A = \frac{1}{6} \bar{v} \rho_0 \frac{\Gamma}{\Delta\nu_D} A, \quad (A2)$$

where $\bar{v} = \sqrt{2kT/m}$ is the mean atomic speed and ρ_0 is the total number density. A factor of $\Gamma/\Delta\nu_D$ is used to count only those atoms which are *on-resonance*.

The value of \mathcal{F} (Eqn. 3 from Section V) is then the ratio of the rate of scattering to the rate of new atoms impinging on the beam, i.e.

$$\begin{aligned} \mathcal{F} &= R/(\Phi A) \\ &= \frac{3r}{\bar{v}\rho_0 l} \frac{\Delta\nu_D}{\Gamma} \left(\frac{I_0}{E_\gamma} \right) \left(1 - \frac{I}{I_0} \right) \\ &\approx 0.022 \quad \text{for this experiment.} \end{aligned} \quad (A3)$$

This approximation agrees with the more detailed analysis, differing only by 10^{-3} .

Appendix B: Linewidth Perturbation

Using the approach and notation of Stace and Luiten [15], the general expression for the absorption coefficient

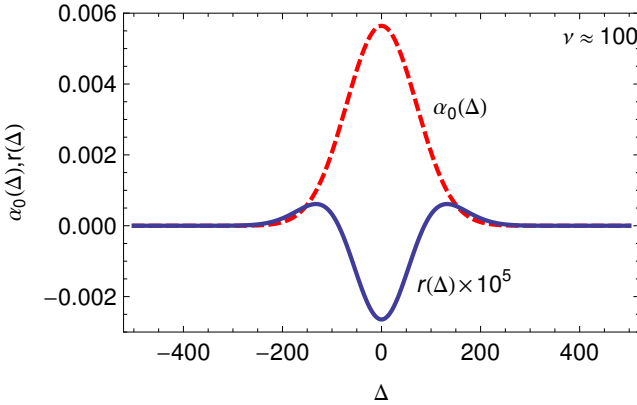


FIG. 7. (Color Online) An example of the unperturbed absorption coefficient ($\alpha_0(\Delta)$) and the additive perturbation term ($r(\Delta)$), plotted for $\nu \approx 30\text{MHz}/3\text{MHz} = 100$. The perturbation term is vertically expanded by 10^5 for clarity. Note that ν in this Appendix has a different meaning to that used in the preceding sections of this paper.

(Eqn. (22) of Ref. [15]) can be expanded (Appendix A1) in the case of small optical pumping. The expression for a perturbed absorption coefficient lineshape is

$$\begin{aligned} \alpha &\approx \frac{\kappa c P_1 z}{2\omega} \left(\left\{ \frac{P_3'' - P_1''}{P_1} \frac{\sqrt{\nu^2 + 1/4}}{8\nu} - \pi \right\} V(\Delta, \nu) \right. \\ &\quad \left. + \frac{P_3'' - P_1''}{P_1} \frac{4(\Delta/\nu)^2 - 3}{64\sqrt{\pi}\nu^3} \exp\left(-\frac{\Delta^2}{\nu^2 + 1/4}\right) \right) \\ &\approx \alpha_0(\Delta) + \epsilon r(\Delta), \end{aligned} \quad (\text{B1})$$

where $\alpha_0(\Delta)$ is the unperturbed lineshape, $r(\Delta)$ is defined as the exponential term in the parentheses and Δ is the detuning in units of the Gaussian width. Fig. (7) shows a plot of the unperturbed lineshape along with the perturbation term $r(\Delta)$. We performed an expansion in the small parameter $\epsilon \equiv (P_3'' - P_1'')/P_1$, where $P_i'' \equiv \partial^2 P_i / \partial \Delta^2$ the derivative is with respect to the de-

tuning Δ . The meanings of the remaining variables in this section are as defined in Ref. [15]. Written in this form, it is clear that the absorption coefficient in the presence of some optical pumping is a Voigt function, denoted $V(\Delta, \nu)$ with an additional perturbation term.

Consider the expansion of a characteristic width for the perturbed absorption coefficient,

$$\Delta_{1/e, \text{pert}}(\epsilon) \approx \Delta_{1/e, \text{pert}}(0) + \frac{d\Delta_{1/e, \text{pert}}}{d\epsilon} \Big|_{\epsilon=0} \delta\epsilon, \quad (\text{B2})$$

such that $\alpha(\Delta_{1/e, \text{pert}})/\alpha(0) \equiv 1/e$. Differentiating this definition and using $\Delta_{1/e, \text{pert}}(0) = \Delta_{1/e}$, we obtain the perturbation to the linewidth

$$\begin{aligned} \frac{d\Delta_{1/e, \text{pert}}}{d\epsilon} \Big|_{\epsilon=0} &= \frac{\alpha_0(0)[r(0)/e - r(\Delta_{1/e})]}{[\alpha_0(0) + \epsilon r(0)][\alpha_0'(\Delta_{1/e}) + \epsilon r'(\Delta_{1/e})]} \\ &\approx \frac{\alpha_0(0)[r(0)/e - r(\Delta_{1/e})]}{\alpha_0 a_0'(\Delta_{1/e})} \\ &\approx -\frac{1/e}{16\sqrt{\pi}\nu^3} \frac{1}{\alpha_0'(\Delta_{1/e})} \\ &\approx -\frac{1}{32\sqrt{\pi}\nu^2}. \end{aligned} \quad (\text{B3})$$

To evaluate $\delta\epsilon$, we have used the low probe power approximation of Stace and Luiten ($P_3 \approx 0 << P_1$) and $\Delta_{1/e} \approx \nu \equiv \Delta\nu_D/\Gamma \approx 100 \gg 1$. We also used the approximate form for the steady-state population density P_1 that ignores atomic coherence. This quantity is maximal on resonance (i.e. when $\Delta = 0$):

$$\begin{aligned} \text{Max}[P_1''] &= P_1''(0) = \frac{d^2}{d\Delta^2} \left(\frac{1}{2} (1 - \exp(-\frac{\Omega^{*2} t^*}{1 + 4\Delta^{*2}})) \right) \Big|_{\Delta=0} \\ &= -4t^* \Omega^{*2} \exp(-t^* \Omega^{*2}) \\ &< -4t^* \Omega^{*2} \\ &\approx -0.4 \quad \text{for this experiment.} \end{aligned}$$

Substitution of the relevant quantities into Eqn. (B2) gives 2 ppm perturbation to the linewidth and, therefore, 4 ppm in the determination of k_B for this experiment.

[1] H. Preston-Thomas. The international temperature scale of 1990. *Metrologia*, 27(1):3–10, 1990.

[2] L. Pitre, M.R. Moldover, and W.L. Tew. Acoustic thermometry: new results from 273 k to 77 k and progress towards 4 k. *Metrologia*, 43(1):142–162, 2006.

[3] Consultative committee for thermometry recommendation t 2 (2005) to the cipm. Online.

[4] B. Fellmuth, C. Gaiser, and J. Fischer. Determination of the boltzmann constant – status and prospects. *Meas. Sci. Tech.*, 17, 2006.

[5] I.M. Mills, P.J. Mohr, T.J. Quinn, B.N. Taylor, and E.R. Williams. Redefinition of the kilogram, ampere, kelvin and mole. *Metrologia*, 43(3):227, 2006.

[6] MR Moldover, JPM Trusler, TJ Edwards, JB Mehl, and RS Davis. Measurement of the universal gas constant r using a spherical acoustic resonator. *PRL*, 60(4):249–252, 1988.

[7] W. Demtröder. *Laser Spectroscopy*. Springer, Berlin, 1981.

[8] A. Unsöld and B. Baschek. *The new cosmos: an introduction to astronomy and astrophysics*. Springer-Verlag, Berlin, 2001.

[9] CJ Bordé. Base units of the SI, fundamental constants and modern quantum physics. *Phil. Trans. R. Soc. A*, 363(1834):2177–2201, 2005.

[10] J Fischer and B Fellmuth. Temperature metrology. *RPP*, 68(5):1043, 2005.

[11] C. Daussy, M. Guinet, A. Amy-Klein, K. Djerroud, Y. Hermier, S. Briaudeau, C.J. Bordé, and C. Chardonnet. Direct determination of the boltzmann constant by

an optical method. *PRL*, 98, 2007.

[12] G. Casa, A. Castrillo, G. Galzerano, R. Wehr, A. Merlone, D. Di Serafino, P. Laporta, and L. Gianfrani. Primary gas thermometry by means of laser-absorption spectroscopy: Determination of the boltzmann constant. *PRL*, 100, 2008.

[13] Antonio Castrillo, Giovanni Casa, Andrea Merlone, Gi-anluca Galzerano, Paolo Laporta, and Livio Gianfrani. On the determination of the boltzmann constant by means of precision molecular spectroscopy in the near-infrared. *Comptes Rendus Physique*, 10(9):894 – 906, 2009.

[14] Khelifa Djerroud, Cyril Lemarchand, Alexandre Gau-guet, Christophe Daussy, Stephan Briaudeau, Benot Dar-qui, Olivier Lopez, Anne Amy-Klein, Christian Chardon-net, and Christian J. Bord. Measurement of the boltz-mann constant by the doppler broadening technique at a 3.810-5 accuracy level. *Comptes Rendus Physique*, 10(9):883 – 893, 2009.

[15] TM Stace and AN Luiten. Theory of spectroscopy in an optically pumped effusive vapor. *PRA*, 81(3):33848, 2010.

[16] Burkhard Wende, editor. *Spectral Line Shapes: Proceedings 5th International Conference*. Walter de Gruyter, Berlin, 1981.

[17] DJ Shin. A novel linearity tester for optical detectors using high-brightness light emitting diodes. *Metrologia*, 42(2):154–158, 2005.

[18] E.D. Black. An introduction to pound–drever–hall laser frequency stabilization. *Am. J. Phys.*, 69:79, 2001.

[19] Michael P. Bradley, James V. Porto, Simon Rainville, James K. Thompson, and David E. Pritchard. Penning trap measurements of the masses of ^{133}Cs , $^{87,85}Rb$, and ^{23}Na with uncertainties ≤ 0.2 ppb. *PRL*, 83(22):4510–4513, 1999.

[20] E. Arimondo, M. Inguscio, and P. Violino. Experimental determinations of the hyperfine structure in the alkali atoms. *Rev. Mod. Phys.*, 49(1):31–75, 1977.

[21] J. Huml̄ek. Optimized computation of the Voigt and complex probability functions. *J. Quant. Spectros. Rad. Trans.*, 27(4):437–444, 1982.

[22] *Igor Pro* ver. 5.0.4.8 Wavemetrics, Inc., Portland, OR., USA.

[23] D.A. Steck. Rubidium 85 d line data. 2008.

[24] J. E. Simsarian, L. A. Orozco, G. D. Sprouse, and W. Z. Zhao. Lifetime measurements of the $7p$ levels of atomic francium. *PRA*, 57(4):2448–2458, Apr 1998.

[25] M. L. Harris, C. S. Adams, S. L. Cornish, I. C. McLeod, E. Tarleton, and I. G. Hughes. Polarization spectroscopy in rubidium and cesium. *Physical Review A (Atomic, Molecular, and Optical Physics)*, 73(6):062509, 2006.

[26] P. Siddons, C.S. Adams, C. Ge, and I.G. Hughes. Ab-solute absorption on the rubidium d lines: compari-sion between theory and experiment. *Arxiv preprint arXiv:0805.1139*, 2008.

[27] A.E. Siegman. *Lasers*. University Science Books, California, 1986.

[28] T. Le Barbu, B. Parvitte, V. Zéninari, I. Vinogradov, O. Koralev, and G. Durry. Diode laser spectroscopy of h 2 o and co 2 in the 1.877- μ m region for the in situ monitoring of the martian atmosphere. *App. Phys. B*, 82(1):133–140, 2006.

[29] H. R. Kratz. The principal series of potassium, rubidium, and cesium in absorption. *Phys. Rev.*, 75(12):1844–1850, Jun 1949.

[30] Lide, editor. *CRC Handbook of Chemistry and Physics*.

[31] N.B. Pilling. Vapor pressure of metallic calcium. *Phys. Rev.*, 18(5):362–368, 1921.

[32] E. Rudberg and J. Lempert. The Vapor Pressure of Bar-ium. *J. Chem. Phys.*, 3:627, 1935.

[33] WP Gilbreath. The vapor pressure of magnesium be-tween 223 and 385 c. *NASA Technical Reports*, 1965.

[34] M. L. Huber, A. Laesecke, and D. G. Friend. The vapor pressure of mercury. *NIST Interagency Reports*, 2006.

[35] X. Xu, T.H. Loftus, J.L. Hall, A. Gallagher, and J. Ye. Cooling and trapping of atomic strontium. *JOSA B*, 20(5):968–976, 2003.

[36] M. Asano and K. Kubo. Vapor Pressure of Strontium below 660 K. *J. Nuc. Sci. Tech.*, 15(10):765–767, 1978.

[37] F. Reif. *Fundamentals of statistical and thermal physics*. McGraw-Hill New York, 1965.